THE JOURNAL OF PHYSICAL CHEMISTRY C

C: Energy Conversion and Storage; Energy and Charge Transport

Three-Dimensional Carbon-Honeycomb as Nano-Porous Lithium and Sodium Deposition Scaffold

Le Shi, Ao Xu, and Tianshou Zhao

J. Phys. Chem. C, **Just Accepted Manuscript** • DOI: 10.1021/acs.jpcc.8b07691 • Publication Date (Web): 25 Aug 2018

Three-Dimensional Carbon-Honeycomb as Nano-Porous Lithium and Sodium Deposition Scaffold

*Le Shi, Ao Xu, Tianshou Zhao**

HKUST Energy Institute, Department of Mechanical and Aerospace Engineering, The Hong Kong University of Science and Technology, Hong Kong, China

*Corresponding author. Tel.: (852) 2358 8647 E-mail: metzhao@ust.hk (T.S. Zhao)

ABSTRACT

Employing density functional theory method, we demonstrate that the recently synthesized three-dimensional carbon-honeycomb (C-honeycomb) can serve as a promising nano-porous scaffold for both lithium and sodium deposition with good electronic conductivity. Lithium/sodium can insert into the channels of C-honeycomb with low migration energy barriers along the walls of one-dimensional pores (<0.5 eV for lithium and <0.25 eV for sodium) and exist in the form of metal nanorods. A high theoretical capacity (711 mAh/g, almost twice of that of graphite) can be achieved when the one-dimensional pores fulfilled with lithium/sodium atoms. The volume expansion of C-honeycomb after metal insertion is less than 5% and 15% for lithium and sodium, respectively. Further introduction of defects such as pyridinic-N doping or single vacancy can provide initial nucleation sites for the metal nanorods and increase the open circuit voltage.

KEY WORDS

Carbon foam; lithium anode; sodium anode; deposition scaffold; Density functional theory (DFT)

1. INTRODUCTION

Along with the development of lithium-based batteries, conventional graphite anodes can no longer provide satisfactory performance for their low theoretical capacity (372 mAh/g). [1] New anode materials with higher capacity, such as silicon and tin, have been proposed and attracted numerous attention in recent years. [2-5] However, as the lithium atoms are stored based on an alloy mechanism, these anode materials suffer from severe volume expansion when providing high capacity, which can cause pulverization of the anode materials and seriously lower the cycle performance. Employment of nanomaterials [6-10] can significantly alleviate the volume expansion and provide longer cycle life, but the resulting volumetric energy density will be much lower and large amount of solid electrolyte interphase (SEI) will be formed due to the large surface area. Therefore, three-dimensional bulk material which can provide high capacity, good electronic conductivity and small volume expansion will be the ideal candidate for lithium anode. On the other hand, sodium-based batteries have been regarded as promising alternatives for lithium-based batteries for the abundance and low price of sodium element. [11-15] Due to the larger atom size, sodium can hardly intercalate into the graphite interlayers and the corresponding capacity is lower than 50 mAh/g. [11] Other possible anode materials, such as phosphorus, suffer from the same problem of large volume expansion as that of alloy-based lithium anode materials. [16-20] Thus, new sodium anode material with high capacity and small volume expansion is urgently needed.

In addition to graphite, various kinds of three-dimensional carbon structures, such as T6- and T14- carbon [21], interpenetration graphene network (IGN) [22], 16-atom body-centered orthorhombic unit cell (bco-C_{16}) [23] and Hex-C_{18} [24] have been predicted based on ab initio calculations. Recently, Krainyukova et al. [25] successfully synthesized a new stable allotrope of carbon named carbon honeycomb (C-honeycomb) via deposition of vacuum-sublimated graphite.

Later, theoretical calculations [26-29] confirmed that the stable C-honeycomb structure is composed of graphene nanoribbons connected by sp^3 carbon atoms as junctions as shown in Figure 1. The C-honeycomb exhibits superior mechanical and thermal properties, and the aligned one-dimensional (1-D) channels in C-honeycomb makes it a promising material for gas adsorption [25] and lithium/sodium storage. As the radius of the 1-D channels of C-honeycomb is much larger than the interlayer spacing of graphite, we propose that different from graphite where lithium atoms intercalate between the interlayers and exist as separated atoms, lithium/sodium atoms may insert into the 1-D channels and nucleate into metal nanorods, thus providing a much higher capacity. The C-honeycomb can be regarded as nano-porous lithium/sodium deposition scaffold. The nanoscale pore size makes it much safer than the micro-porous lithio/sodio-philic frameworks [30-33] where lithium/sodium can form large scale continuous phase.

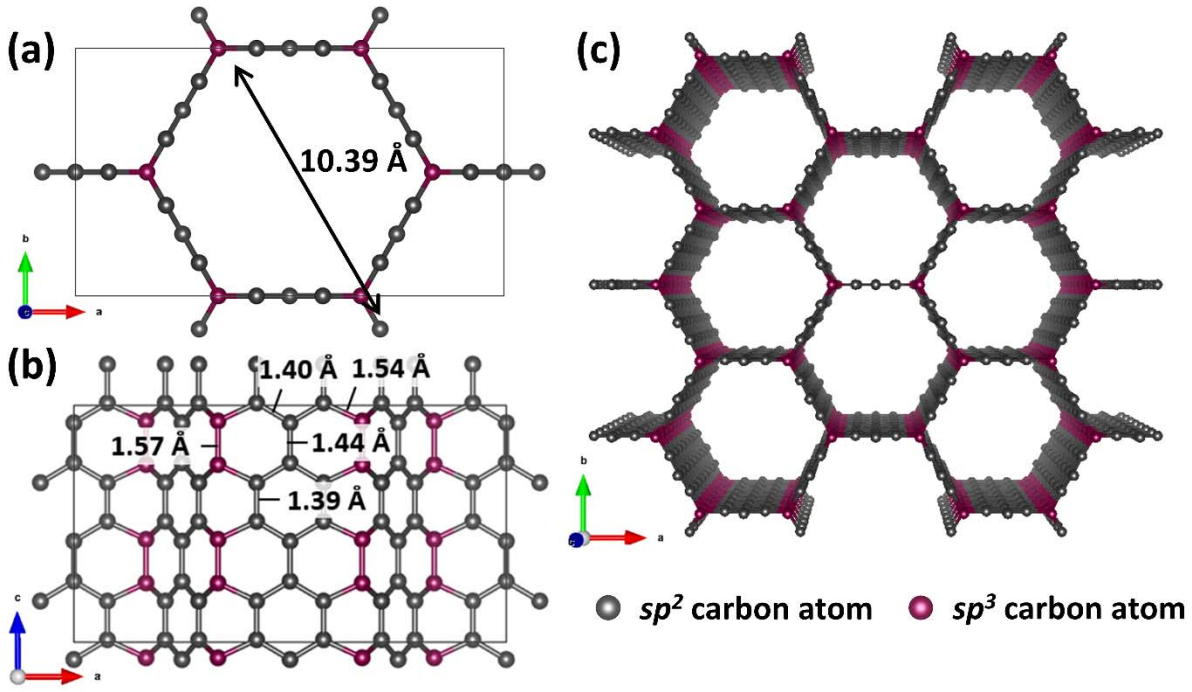

Figure 1. The geometry of C-honeycomb from (a) side (b)top and (c) perspective view

2. COMPUTATIONAL METHODOLOGY

All the computations were performed using Abinit [34-36] software package, with Perdew-Burke-Ernzerhof (PBE) generalized gradient approximation (GGA) [37] and the projector augmented wave (PAW) method. [38] Grimme's DFT-D2 [39] correction was adopted to account for the van der Waals interaction. The cut-off energy was set to be 20 Ha. The k-point mesh was set to be < 0.06 $Å^{-1}$ for geometry optimization and <0.03 $Å^{-1}$ for the calculation of density of states. All the structures were fully optimized to a force tolerance of 0.01 eV $Å^{-1}$. The migration energy barriers of lithium/sodium inside the C-honeycomb were calculated using climbing image nudged elastic band (CI-NEB) method [40], and fifteen images were used. The binding energies were calculated as [41]:

$$E_{bind} = (E_{C-h+M} - E_{C-h} - n\mu_M)/n \quad (1)$$

and the adsorption energies were calculated as

$$E_{ads} = (E_{C-h+M} - E_{C-h} - nE_M)/n \quad (2)$$

where the E_{C-h+M} is the total energy of lithium/sodium atoms adsorbed on C-honeycomb, E_{C-h} is the total energy of C-honeycomb, n is the number of lithium/sodium adsorbed, μ_M is the chemical potential of metallic lithium/sodium, and E_M is the energy of a single lithium/sodium atom. The open circuit voltage was estimated by [41]:

$$\text{OCV} \approx [E_{Mx_1C-h} - E_{Mx_2C-h} + (x_2 - x_1)\mu_M]/(x_2 - x_1)e \quad (3)$$

where E_{Mx_1C-h} and E_{Mx_2C-h} means the total energy of C-honeycomb adsorbed with x_1 and x_2 lithium/sodium atoms.

3. RESULTS AND DISCUSSION

3.1 Geometry and electronic conductivity of carbon-honeycomb

We optimized the geometry of C-honeycomb based on the structure proposed by Pang et al. [26], and 6-6-6 sp^3 junction was chosen instead of the 5-5-8 junction for the lower cohesive energy. [26, 27] A 1×1×2 supercell consists of 88 carbon atoms was adopted for further calculations. The detailed geometry of the optimized C-honeycomb is shown in Figure 1, and the diameter of the 1-D channels is about 1 nm. In addition to the pristine C-honeycomb, the C-honeycomb may also accommodate the same type of defects as graphene at little energy cost as predicted by Zhu and Tománek [42]. Thus, we further considered the influence of pyridinic-N doping and formation of single vacancy towards the performance of C-honeycomb as anode material (illustrated in Figure 2(a1) and (a2)). The calculated density of states (DOS) in Figure 2(b) shows that the pristine C-honeycomb exhibits a small bandgap of about 0.5 eV, while after the introduction of pyridinic-N doping or single vacancy, the density of states at Fermi level become a positive value, which indicates better electronic conductivity. These results ensure that the C-honeycomb can provide sufficient electronic conductivity when serving as lithium/sodium anode material.

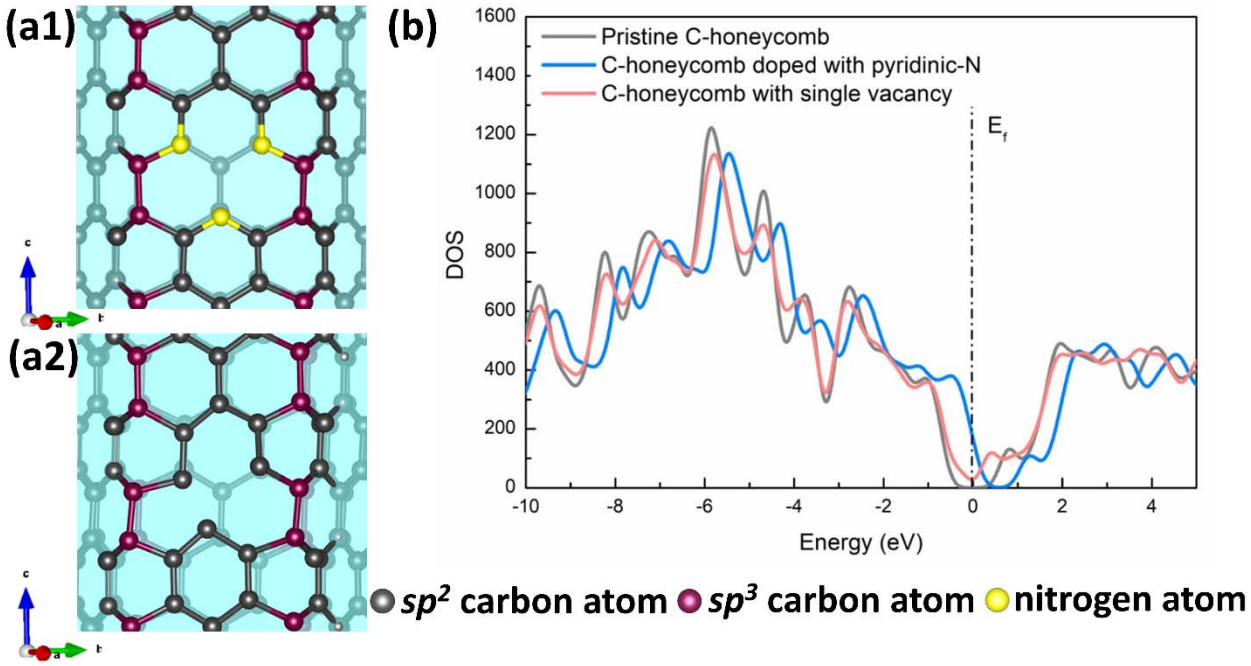

Figure 2. The geometry of (a1) pyridinic-N doping and (a2) single vacancy. (b) The density of states of pristine C-honeycomb, C-honeycomb doped with pyridinic-N and C-honeycomb with single vacancy, where the dashed line represents the Fermi level.

3.2 Lithium/sodium insertion into carbon-honeycomb

Then the binding energies of lithium/sodium at different concentrations on the C-honeycomb were calculated. For single lithium/sodium atom, several possible lithium/sodium adsorption sites on pristine C-honeycomb were studied as shown in Figure S2. From the binding energies listed in Table S2, the interaction between lithium/sodium atoms and C-honeycomb are relatively weak and the binding energies are positive, similar with the case on pristine graphene [43]. Then we tried to increase the lithium/sodium insertion concentration. Based on the size of nanochannel, the highest amount of lithium/sodium that can be inserted is $(Li/Na)_{28}C_{88}$, corresponding to a capacity of 711 mAh/g. Two packing forms of lithium/sodium inside the channels were considered. The first one named “hexagonal form” was constructed based on the

most stable single atom adsorption site, where six lithium/sodium atoms were attached to their most stable adsorption site on the wall, then another lithium/sodium atom sit ahead of the hexagonal ring formed as shown in Figure S3(a). The second one named “cubic form” was constructed based on the bulk structure of lithium/sodium metal, where the lithium/sodium atoms packed in the same way of their bulk form as shown in Figure S3(b)(c). After geometrical optimization, the hexagonal packing form is unstable for sodium and will transform into cubic form during the structural optimization process. The perspective view of C-honeycomb after 50% and 100% lithium/sodium insertion is shown in Figure 3. For lithium packed in cubic form inside C-honeycomb, the C-honeycomb will go through a significant structural deformation, where the C-honeycomb lattice parallel to the direction packed with more lithium atoms will elongate. As shown in Figure 4, After the insertion of 50% lithium/sodium, the binding energies will be reduced compared with the single atom cases, and the lithium binding energy will become negative, suggesting that the insertion of lithium into the C-honeycomb channels at high concentration is thermodynamically favorable compared with forming segregated lithium phase. After the insertion of 100% lithium/sodium, the binding energies will be further reduced and the sodium binding energy will become very close to zero (+0.01 eV). The reduced binding energy come from the cohesive energy of metal packing, and the cubic form packing is more stable compared with the hexagonal form, thus contributed more cohesive energy and resulted in lower binding energy.

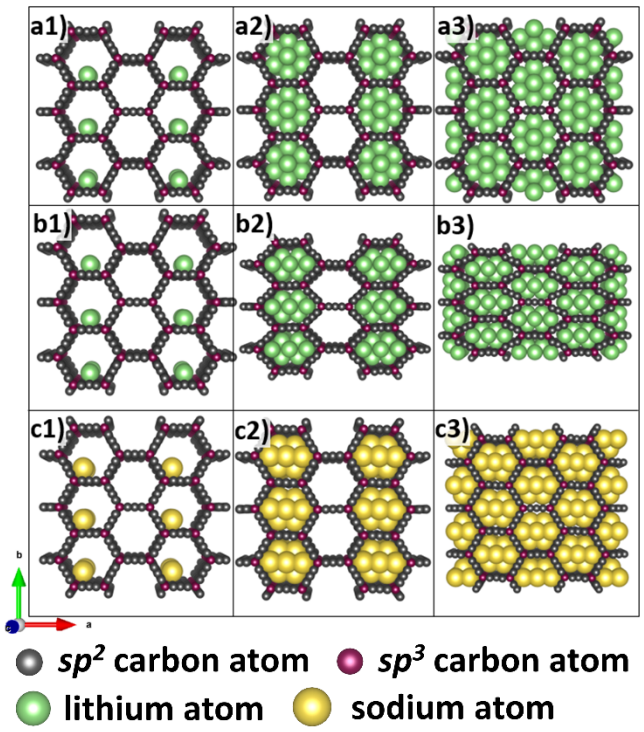

Figure 3. The perspective view of a 1×1×2 pristine C-honeycomb supercell filled with (a1)-(a3) 1,14 and 28 lithium atoms packed in hexagonal form; (b1)-(b3) 1, 14 and 28 lithium atoms packed in cubic form; (c1)-(c3) 1, 14 and 28 sodium atoms packed in cubic form

The pristine C-honeycomb can provide negative binding energies towards lithium at high concentrations, but cannot stabilize the adsorption of single lithium atom and sodium atoms at all concentrations. Introduction of defects such as nitrogen doping or vacancy has been proven to be an effective strategy to enhance the interaction between metal atoms and graphene basal plane [44-46]. Therefore, we start to study the lithium/sodium binding onto defective C-honeycomb. In addition to the pyridinic-N doping and single vacancy mentioned above, graphitic-N doping was also studied as shown in Figure S4. However, from the calculated binding energies as listed in Table S3, the graphitic-N doping shows little influence towards the binding energies, thus it is not considered for further discussions. The other form of reported N-doping, the pyrrolic-N doping,

requires larger graphene nanoribbons and cannot be properly constructed in our case. [47] Figure S6-S11 show the geometries of lithium/sodium insertion inside C-honeycomb with pyridinic-N doping and single vacancy. The most stable binding site will change due to the introduction of defects and the packing form will be altered slightly. Figure S12 shows the electron distribution of C-honeycomb doped with pyridinic-N and C-honeycomb with single vacancy. It is found that the introduction of these defects creates an electron deficient area in the C-honeycomb, which can help trap the lithium/sodium atoms. Figure S13 and S14 show the charge transfer between adsorbed lithium/sodium and pristine C-honeycomb, C-honeycomb doped with pyridinic-N and C-honeycomb with single vacancy. It is found that the area involved in the charge transfer process become larger after the introduction of pyridinic-N doping and single vacancy, which may explain the stronger adsorption behavior.

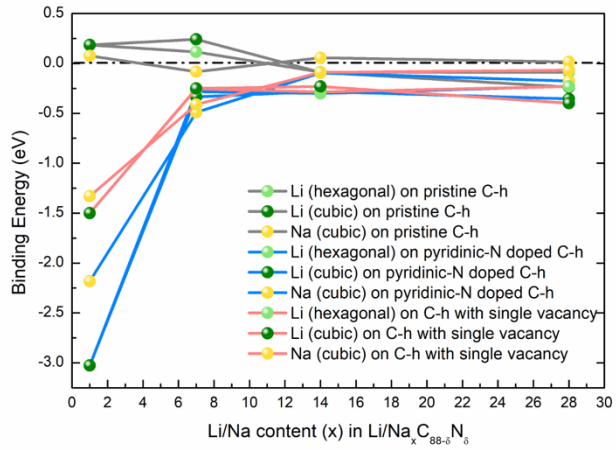

Figure 4. The binding energies of lithium/sodium onto pristine and defective C-honeycomb (C-h) at different concentrations

The binding energies of lithium/sodium on defective C-honeycomb at different concentrations can be found in Figure 4. For single lithium/sodium atom, the binding energy will be greatly lowered after the introduction of pyridinic-N doping or single vacancy. With more

lithium/sodium inserted, the influence of defects will be averaged, making the binding energies higher but still negative. These results show that the introduction of defects such as pyridinic-N doping or single vacancy is necessary to lure the lithium/sodium atoms insert into the C-honeycomb channels. Afterwards the inserted lithium/sodium atoms will be trapped on the defect sites and serve as nucleation site for metal nanorod growth. A small number of defects (3.4% pyridinic-N doping or 1.1% single vacancy) can ensure that the whole insertion process is thermodynamically favorable, which can be realized in experiments easily [48-53].

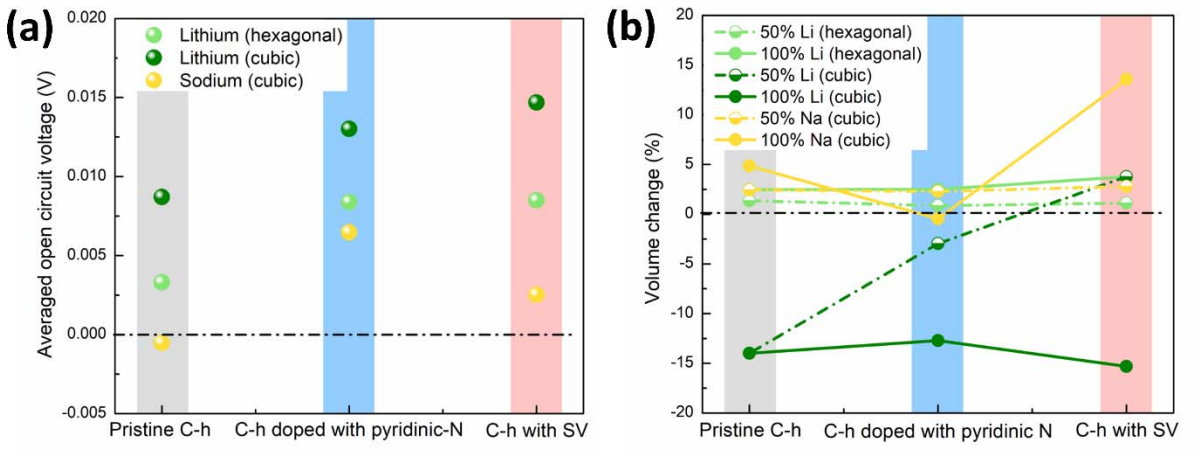

Figure 5. (a) The averaged open circuit voltage of pristine C-honeycomb (C-h), C-honeycomb doped with pyridinic-N and C-honeycomb with single vacancy as the anode material for lithium- and sodium-ion batteries (b) The volume change of pristine C-honeycomb, C-honeycomb doped with pyridinic-N and C-honeycomb with single vacancy when filled with 50% and 100% lithium or sodium atoms. The symbols in Figure 5(b) were linked to guide the eyes.

The calculated averaged open circuit voltage (OCV) of pristine and defective C-honeycomb is shown in Figure 5 (a). Except the case for sodium on pristine C-honeycomb, all the OCVs are small positive values, which is similar with that of graphite [54]. The small positive

OCVs will ensure the insertion of lithium/sodium inside the C-honeycomb channels and provide a large cell voltage. The volume expansion after lithium/sodium insertion is shown in Figure 5(b). For lithium packed in hexagonal form, the volume shows very slight change within 5%, while for lithium packed in cubic form, the volume shrinks about 15% when the channels are fully filled due to the structural deformation mentioned above. For sodium, the volume expansion is within 15% for all the cases. The detailed lattice parameter changes can be found in Figure S15-S20.

3.3 Lithium/sodium migration inside carbon-honeycomb

We then calculated the migration energy barriers of lithium and sodium inside the channels of C-honeycomb. Two migration pathways were considered for both cases as shown in Figure 6 (a)(b), path A is that the lithium/sodium atom directly migrate from one most stable adsorption site to the next most stable adsorption site (Wall1→Wall1 for lithium and Wall2→Wall2 for sodium), and path B is that the lithium/sodium first migrate to the nearest meta-stable adsorption site, and then migrate to the other most stable adsorption site (Wall1→Wall2→Wall1 for lithium and Wall2→Wall1→Wall2 for sodium). From Figure 6(c), the migration energy barriers are smaller than 0.5 eV for lithium and smaller than 0.25 eV for sodium, similar with our previous results on lithium/sodium migration energy barriers on pristine graphene [43]. These small energy barriers indicate that lithium/sodium atoms can migrate fast inside the 1-D channels during discharge/charge process, thus provide a good rate capability.

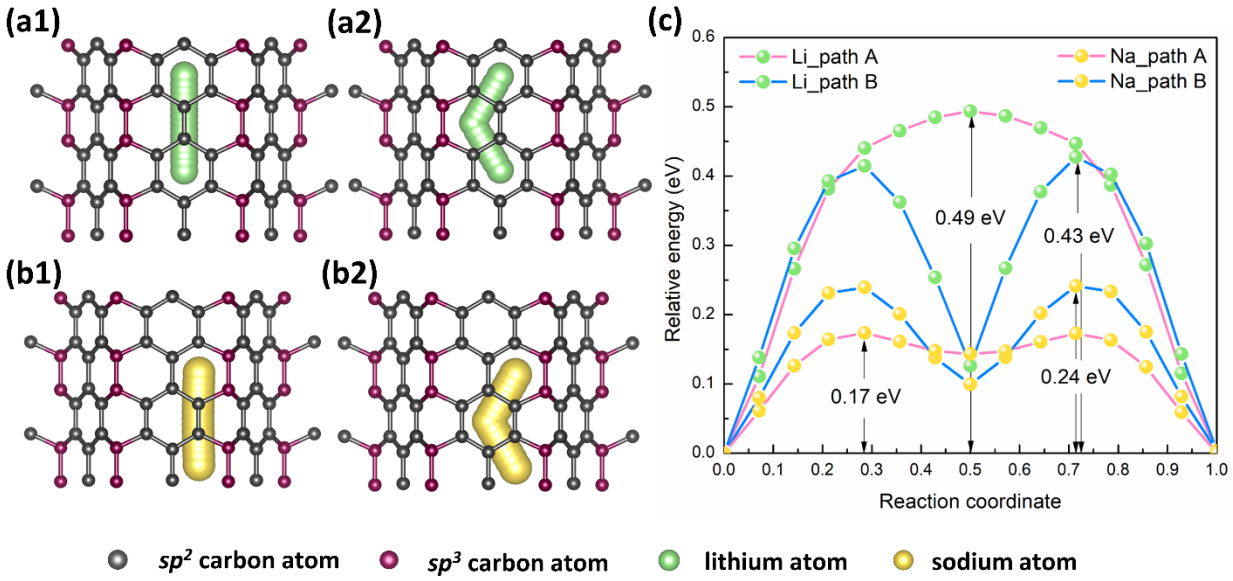

Figure 6. Lithium migration along C-honeycomb channels following (a1) path A and (a2) path B; sodium migration along C-honeycomb following (b1) path A and (b2) path B; (c) The migration energy barriers for lithium/sodium in C-honeycomb

It is worth mentioning that in addition to the C-honeycomb structure discussed in this work, there exist many other kinds of possible 3-D carbon network structures made up of graphene nanoribbon array and junctions. [55-58] We expect these 3-D carbon networks share similar electrochemical properties with the C-honeycomb discussed here when serving as lithium/sodium anode materials. Moreover, with larger pore radius, the theoretical capacity can be further increased and the binding energies at high lithium/sodium concentrations can be further lowered.

4. CONCLUSION

In conclusion, we explored the feasibility of using the recently synthesized C-honeycomb as nano-porous scaffold for lithium/sodium deposition using density functional theory method. Calculation results show that lithium/sodium can insert into the 1-D channels of C-honeycomb with low migration energy barriers and packed inside as metal nanorods, thus providing a high

capacity of 711 mAh/g. Introduction of defects such as pyridinic-N doping or single vacancy can significantly lower the binding energies at low lithium/sodium concentrations and provide nucleation sites for further lithium/sodium insertion. Other possible 3-D carbon networks sharing similar structure with C-honeycomb may also be promising lithium/sodium anode materials with even higher capacity depending on their pore size. We hope these results will provide new direction to the searching of lithium/sodium anode materials.

ACKNOWLEDGEMENTS

The work described in this paper was supported by a grant from the Research Grants Council of the Hong Kong Special Administrative Region, China (Project No. T23-601/17-R).

REFERENCES

[1] Wu, Y. P.; Rahm, E.; Holze, R. Carbon Anode Materials for Lithium Ion Batteries. *J. Power Sources* **2003**, *114*, 228-236.

[2] Zhang, W. J. A Review of the Electrochemical Performance of Alloy Anodes for Lithium-Ion Batteries. *J. Power Sources* **2011**, *196*, 13-24.

[3] Scrosati, B.; Hassoun, J.; Sun, Y. K. Lithium-Ion Batteries. A Look into the Future. *Energy Environ. Sci*. **2011**, *4*, 3287-3295.

[4] Wachtler, M.; Besenhard, J. O.; Winter, M. Tin and Tin-Based Intermetallics as New Anode Materials for Lithium-Ion Cells. *J. Power Sources* **2001**, *94*, 189-193.

[5] Zhang, W. J. Lithium Insertion/Extraction Mechanism in Alloy Anodes for Lithium-Ion Batteries. *J. Power Sources* **2011**, *196*, 877-885.

[6] Shi, L.; Zhao, T. Recent Advances in Inorganic 2D Materials and Their Applications in Lithium and Sodium Batteries. *J. Mater. Chem. A* **2017**, *5*, 3735-3758.

[7] Magasinski, A.; Dixon, P.; Hertzberg, B.; Kvit, A.; Ayala, J.; Yushin, G. High-Performance Lithium-Ion Anodes Using A Hierarchical Bottom-Up Approach. *Nat. Mater*. **2010**, *9*, 353.

[8] Zhang, W. M.; Hu, J. S.; Guo, Y. G.; Zheng, S. F.; Zhong, L. S.; Song, W. G.; Wan, L. J. Tin-Nanoparticles Encapsulated in Elastic Hollow Carbon Spheres for High-Performance Anode Material in Lithium-Ion Batteries. *Adv. Mater*. **2008**, *20*, 1160-1165.

[9] Zhou, J.; Qin, J.; Zhang, X.; Shi, C.; Liu, E.; Li, J.; Zhao, N.; He, C. 2D Space-Confined Synthesis of Few-Layer MoS_2 Anchored on Carbon Nanosheet for Lithium-Ion Battery Anode. *ACS Nano* **2015**, *9*, 3837-3848.

[10] Qin, J.; He, C.; Zhao, N.; Wang, Z.; Shi, C.; Liu, E. Z.; Li, J. Graphene Networks Anchored with Sn@ Graphene as Lithium Ion Battery Anode. *ACS Nano* **2014**, *8*, 1728-1738.

[11] Slater, M. D.; Kim, D.; Lee, E.; Johnson, C. S. Sodium-Ion Batteries. *Adv. Funct. Mater*. **2013**, *23*, 947-958.

[12] Ellis, B. L.; Nazar, L. F. Sodium and Sodium-Ion Energy Storage Batteries. *Curr. Opin. Solid State Mater. Sci*. **2012**, *16*, 168-177.

[13] Yabuuchi, N.; Kubota, K.; Dahbi, M.; Komaba, S. Research Development on Sodium-Ion Batteries. *Chem. Rev*. **2014**, *114*, 11636-11682.

[14] Xin, S.; Yin, Y. X.; Guo, Y. G.; Wan, L. J. A High-Energy Room-Temperature Sodium-Sulfur Battery. *Adv. Mater*. **2014**, *26*, 1261-1265.

[15] Das, S. K.; Lau, S.; Archer, L. A. Sodium–Oxygen Batteries: A New Class of Metal–Air Batteries. *J. Mater. Chem. A.* **2014**, *2*, 12623-12629.

[16] Qian, J.; Wu, X.; Cao, Y.; Ai, X.; Yang, H. High Capacity and Rate Capability of Amorphous Phosphorus for Sodium Ion Batteries. *Angew. Chem. Int. Ed*. **2013**, *125*, 4731-4734.

[17] Zhu, Y.; Wen, Y.; Fan, X.; Gao, T.; Han, F.; Luo, C.; Liou, S. C.; Wang, C. Red Phosphorus–Single-Walled Carbon Nanotube Composite as A Superior Anode for Sodium Ion Batteries. *ACS Nano* **2015**, *9*, 3254-3264.

[18] Zhang, C.; Wang, X.; Liang, Q.; Liu, X.; Weng, Q.; Liu, J.; Yang, Y.; Dai, Z.; Ding, K.; Bando, Y.; Tang, J. Amorphous Phosphorus/Nitrogen-Doped Graphene Paper for Ultrastable Sodium-Ion Batteries. *Nano Lett*. **2016**, *16*, 2054-2060.

[19] Shi, L.; Zhao, T.; Xu, A.; Xu, J. Ab Initio Prediction of Borophene as An Extraordinary Anode Material Exhibiting Ultrafast Directional Sodium Diffusion for Sodium-Based Batteries. *Sci. Bull*. **2016**, *61*, 1138-1144.

[20] Sun, J.; Lee, H. W.; Pasta, M.; Yuan, H.; Zheng, G.; Sun, Y.; Li, Y.; Cui, Y. A Phosphorene–Graphene Hybrid Material as A High-Capacity Anode for Sodium-Ion Batteries. *Nat. Nanotechnol*. **2015**, *10*, 980.

[21] Zhang, S; Wang, Q.; Chen, X.; Jena, P. Stable Three-Dimensional Metallic Carbon with Interlocking Hexagons. *Proc. Natl. Acad. Sci*. **2013**, *110*, 18809-18813.

[22] Chen, Y.; Xie, Y.; Yang, S. A.; Pan, H.; Zhang, F.; Cohen, M. L.; Zhang, S. Nanostructured Carbon Allotropes with Weyl-like Loops and Points. *Nano Lett*. **2015**, *15*, 6974-6978.

[23] Wang, J. T.; Weng, H.; Nie, S.; Fang, Z.; Kawazoe, Y.; Chen, C. Body-Centered Orthorhombic C_{16}: A Novel Topological Node-Line Semimetal. *Phys. Rev. Lett*. **2016**, *116*, 195501.

[24] Liu, J.; Zhao, T.; Zhang, S.; Wang Q. A New Metallic Carbon Allotrope with High Stability and Potential for Lithium Ion Battery Anode Material. *Nano Energy* **2017**, *38*, 263-270.

[25] Krainyukova, N. V.; Zubarev, E. N. Carbon Honeycomb High Capacity Storage for Gaseous and Liquid Species. *Phys. Rev. Lett*. **2016**, *116*, 055501.

[26] Pang, Z.; Gu, X.; Wei, Y.; Yang, R.; Dresselhaus, M. S. Bottom-Up Design of Three-Dimensional Carbon-Honeycomb with Superb Specific Strength and High Thermal Conductivity. *Nano Lett*. **2016**, *17*, 179-185.

[27] Gu, X.; Pang, Z.; Wei, Y.; Yang, R. On the Influence of Junction Structures on the Mechanical and Thermal Properties of Carbon Honeycombs. *Carbon*. **2017**, *119*, 278-286.

[28] Gao, Y.; Chen, Y.; Zhong, C.; Zhang, Z.; Xie, Y.; Zhang, S. Electron and Phonon Properties and Gas Storage in Carbon Honeycombs. *Nanoscale* **2016**, *8*, 12863-12868.

[29] Fthenakis, Z. G. Are the Experimentally Observed 3-Dimensional Carbon Honeycombs All-sp^2 Structures? The Dangling p-Orbital Instability. *RSC Adv*. **2017**, *7*, 9790-9794.

[30] Zhang, R.; Li, N. W.; Cheng, X. B.; Yin, Y. X.; Zhang, Q.; Guo, Y. G. Advanced Micro/Nanostructures for Lithium Metal Anodes. *Adv. Sci*. **2017**, *4*, 1600445.

[31] Chi, S. S.; Qi, X. G.; Hu, Y. S.; Fan, L. Z. 3D Flexible Carbon Felt Host for Highly Stable Sodium Metal Anodes. *Adv. Energy Mater*. **2018**, 1702764.

[32] Zhu, M.; Li, B.; Li, S.; Du, Z.; Gong, Y.; Yang, S. Dendrite-Free Metallic Lithium in Lithiophilic Carbonized Metal-Organic Frameworks. *Adv. Energy Mater*. **2018**, 1703505.

[33] Zhang, R.; Chen, X. R.; Chen, X.; Cheng, X. B.; Zhang, X. Q.; Yan, C.; Zhang, Q. Lithiophilic Sites in Doped Graphene Guide Uniform Lithium Nucleation for Dendrite-Free Lithium Metal Anodes. *Angew. Chem. Int. Ed*. **2017**, *56*, 7764-7768.

[34] Gonze, X.; Beuken, J. M.; Caracas, R.; Detraux, F.; Fuchs, M.; Rignanese, G. M.; Sindic, L.; Verstraete, M.; Zerah, G.; Jollet, F.; Torrent, M. First-Principles Computation of Material Properties: the ABINIT Software Project. *Comput. Mater. Sci*. **2002**, *25*, 478-492.

[35] Gonze, X.; Amadon, B.; Anglade, P. M.; Beuken, J. M.; Bottin, F.; Boulanger, P.; Bruneval, F.; Caliste, D.; Caracas, R.; Côté, M.; Deutsch, T. ABINIT: First-Principles Approach to Material and Nanosystem Properties. *Comput. Phys. Commun*. **2009**, *180*, 2582-2615.

[36] Gonze, X. A Brief Introduction to the ABINIT Software Package. *Z. Kristallogr. - Cryst. Mater*. **2005**, *220*, 558-562.

[37] Perdew, J. P.; Burke, K.; Ernzerhof, M. Generalized Gradient Approximation Made Simple. *Phys. Rev. Lett*. **1996**, *77*, 3865.

[38] Blöchl, P. E. Projector Augmented-Wave Method. *Phys. Rev. B*. **1994**, *50*, 17953.

[39] Grimme, S. Semiempirical GGA-Type Density Functional Constructed with A Long-Range Dispersion Correction. *J. Comput. Chem*. **2006**, *27*, 1787-1799.

[40] Henkelman, G.; Uberuaga, B. P.; Jónsson, H. A Climbing Image Nudged Elastic Band Method for Finding Saddle Points and Minimum Energy Paths. *J. Chem. Phys*. **2000**, *113*, 9901-9904.

[41] Jing, Y.; Zhou, Z.; Cabrera, C. R.; Chen, Z. Metallic VS_2 Monolayer: A Promising 2D Anode Material for Lithium Ion Batteries. *J. Phys. Chem. C* **2013**, *117*, 25409-25413.

[42] Zhu, Z.; Tománek, D. Formation and Stability of Cellular Carbon Foam Structures: An ab initio Study. *Phys. Rev. Lett*. **2012**, *109*, 135501.

[43] Shi, L.; Zhao, T. S.; Xu, A.; Xu, J. B. Ab initio Prediction of a Silicene and Graphene Heterostructure as An Anode Material for Li-and Na-Ion Batteries. *J. Mater. Chem. A*. **2016**, *4*, 16377-16382.

[44] Xu, J.; Wang, M.; Wickramaratne, N. P.; Jaroniec, M.; Dou, S.; Dai, L. High-Performance Sodium Ion Batteries Based on a 3D Anode from Nitrogen-Doped Graphene Foams. *Adv. Mater.* **2015**, *27*, 2042-2048.

[45] Er, D.; Detsi, E.; Kumar, H.; Shenoy, V. B. Defective Graphene and Graphene Allotropes as High-Capacity Anode Materials for Mg Ion Batteries. *ACS Energy Lett*. **2016**, *1*, 638-645.

[46] Mukherjee, R.; Thomas, A. V.; Datta, D.; Singh, E.; Li, J.; Eksik, O.; Shenoy, V. B.; Koratkar, N. Defect-Induced Plating of Lithium Metal within Porous Graphene Networks. *Nat. Commun*. **2014**, *5*, 3710.

[47] Jing, Y.; Zhou, Z. Computational Insights into Oxygen Reduction Reaction and Initial Li_2O_2 Nucleation on Pristine and N-Doped Graphene in Li–O_2 Batteries. *ACS Catal*. **2015**, *5*, 4309-4317.

[48] Guo, D; Shibuya, R.; Akiba, C.; Saji, S.; Kondo, T.; Nakamura, J. Active Sites of Nitrogen-Doped Carbon Materials for Oxygen Reduction Reaction Clarified Using Model Catalysts. *Science*. **2016**, *351*, 361-365.

[49] Jiang, K.; Eitan, A.; Schadler, L. S.; Ajayan, P. M.; Siegel, R. W.; Grobert, N.; Mayne, M.; Reyes-Reyes, M.; Terrones, H.; Terrones, M. Selective Attachment of Gold Nanoparticles to Nitrogen-Doped Carbon Nanotubes. *Nano Lett*. **2003**, *3*, 275-277.

[50] Liang, H. W.; Wei, W.; Wu, Z. S.; Feng, X.; Müllen, K. Mesoporous Metal-Nitrogen-Doped Carbon Electrocatalysts for Highly Efficient Oxygen Reduction Reaction. *J. Am. Chem. Soc*. **2013**, *135*, 16002-16005.

[51] Tang, Y.; Allen, B. L.; Kauffman, D. R.; Star, A. Electrocatalytic Activity of Nitrogen-Doped Carbon Nanotube Cups. *J. Am. Chem. Soc*. **2009**, *131*, 13200-13201.

[52] Mawhinney, D. B.; Naumenko, V.; Kuznetsova, A.; Yates, Jr. J. T.; Liu, J.; Smalley, R. E. Surface Defect Site Density on Single Walled Carbon Nanotubes by Titration. *Chem. Phys. Lett*. **2000**, *324*, 213-216.

[53] Hao, F.; Fang, D.; Xu, Z. Mechanical and Thermal Transport Properties of Graphene with Defects. *Appl. Phys. Lett*. **2011**, *99*, 041901.

[54] Okamoto, Y. Density Functional Theory Calculations of Alkali Metal (Li, Na, and K) Graphite Intercalation Compounds. *J. Phys. Chem. C*. **2013**, *118*, 16-19.

[55] Wu, M.; Wu, X.; Pei, Y.; Wang, Y.; Zeng, X. C. Three-Dimensional Network Model of Carbon Containing Only sp^2-Carbon Bonds and Boron Nitride Analogues. *Chem. Commun*. **2011**, *47*, 4406-4408.

[56] Zhang, J. Negative Poisson's Ratio in Graphene-Based Carbon Foams. *Phys. Chem. Chem. Phys*. **2018**, *20*, 4597-4605

[57] Han, Y.; Yang, J. Y.; Hu, M. Unusual Strain Response of Thermal Transport in Dimerized Three-Dimensional Graphene. *Nanoscale* **2018**, *10*, 5229-5238.

[58] Gao, X.; Shen, X. Face-to-Face Crosslinking of Graphdiyne and Related Carbon Sheets toward Integrated Graphene Nanoribbon Arrays. *Carbon* **2017**, *125*, 536-543.

TOC GRAPHICS

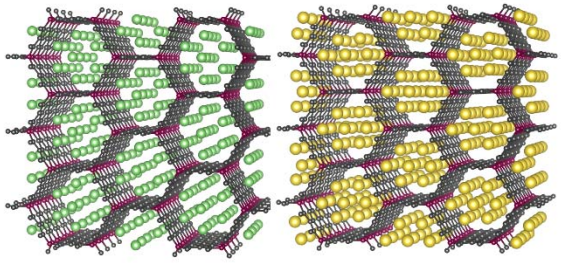

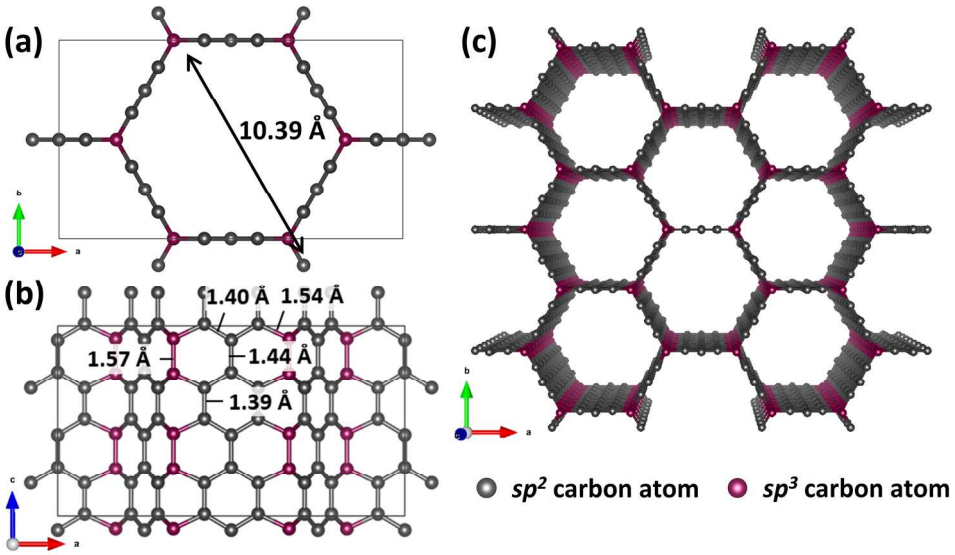

The geometry of C-honeycomb from (a) side (b)top and (c) perspective view

99x56mm (600 x 600 DPI)

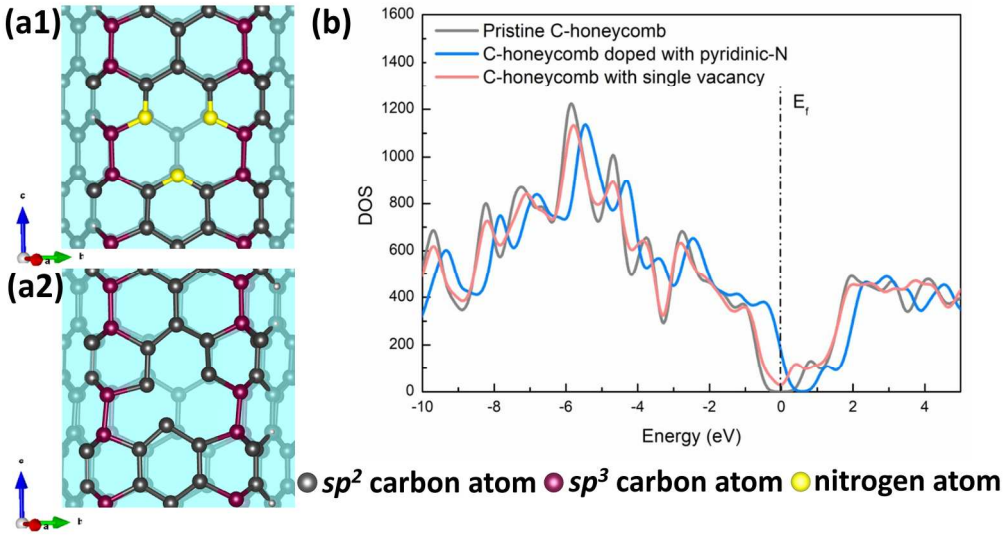

The geometry of (a1) pyridinic-N doping and (a2) single vacancy. (b) The density of states of pristine C-honeycomb, C-honeycomb doped with pyridinic-N and C-honeycomb with single vacancy, where the dashed line represents the Fermi level.

99x56mm (600 x 600 DPI)

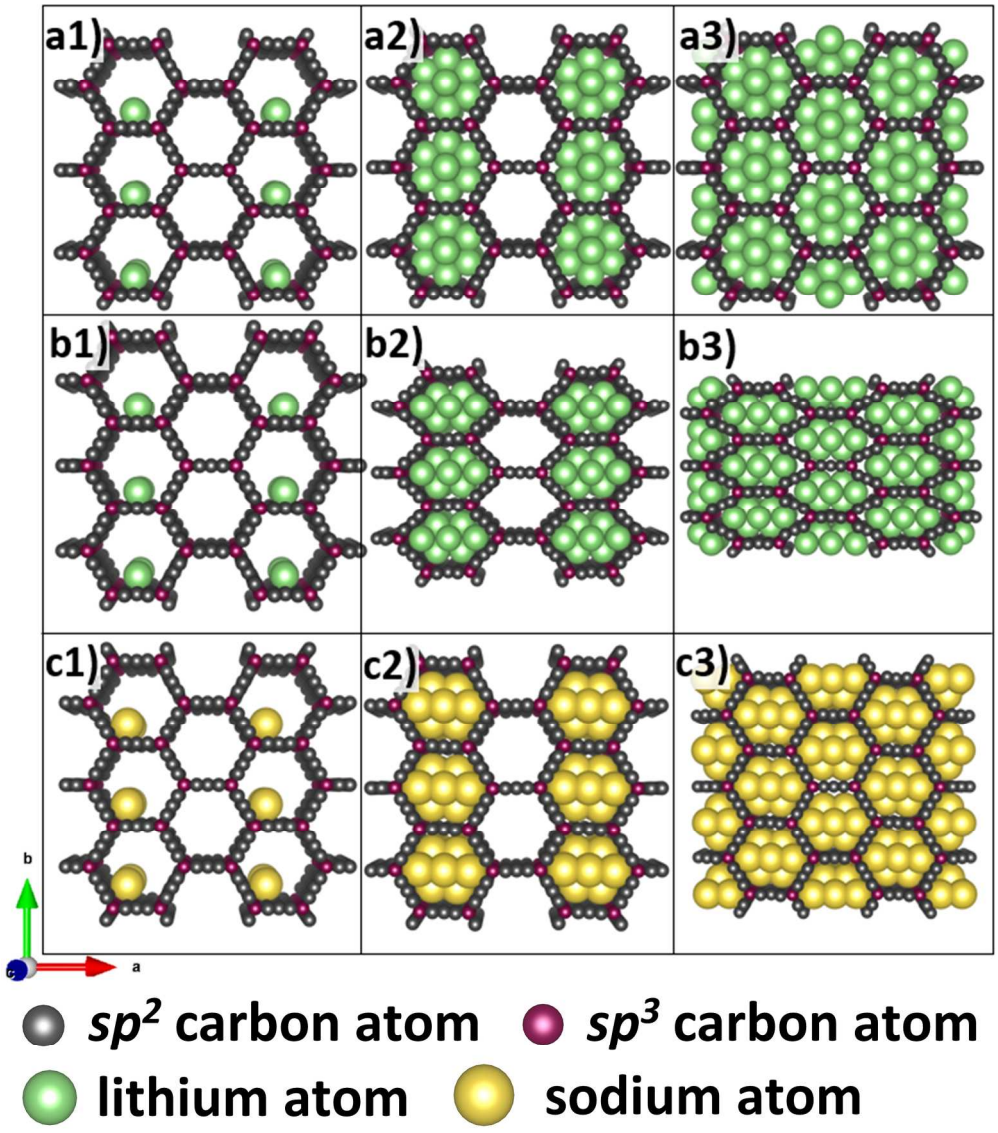

The perspective view of a 1×1×2 pristine C-honeycomb supercell filled with (a1)-(a3) 1,14 and 28 lithium atoms packed in hexagonal form; (b1)-(b3) 1, 14 and 28 lithium atoms packed in cubic form; (c1)-(c3) 1, 14 and 28 sodium atoms packed in cubic form

99x117mm (600 x 600 DPI)

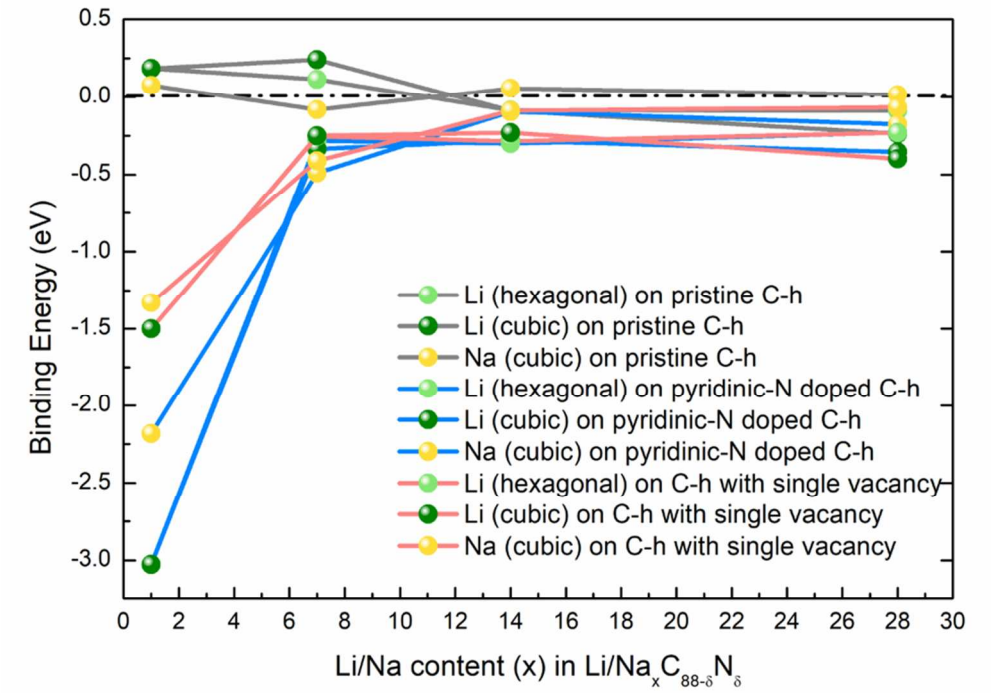

The binding energies of lithium/sodium onto pristine and defective C-honeycomb (C-h) at different concentrations

59x42mm (600 x 600 DPI)

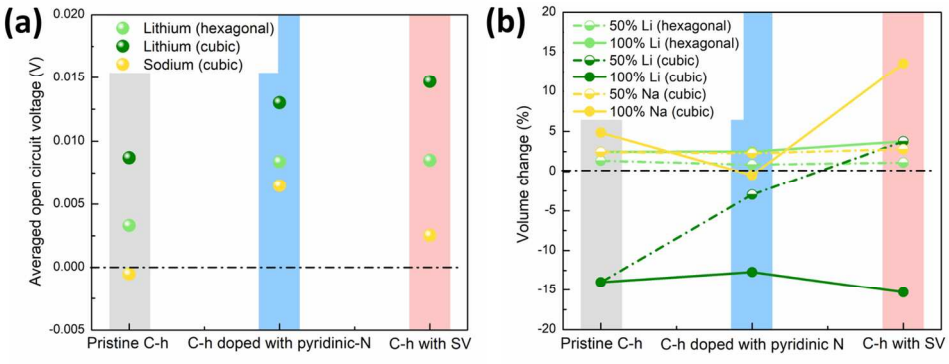

(a) The averaged open circuit voltage of pristine C-honeycomb (C-h), C-honeycomb doped with pyridinic-N and C-honeycomb with single vacancy as the anode material for lithium- and sodium-ion batteries (b) The volume change of pristine C-honeycomb, C-honeycomb doped with pyridinic-N and C-honeycomb with single vacancy when filled with 50% and 100% lithium or sodium atoms. The symbols in Figure 5(b) were linked to guide the eyes

74x31mm (600 x 600 DPI)

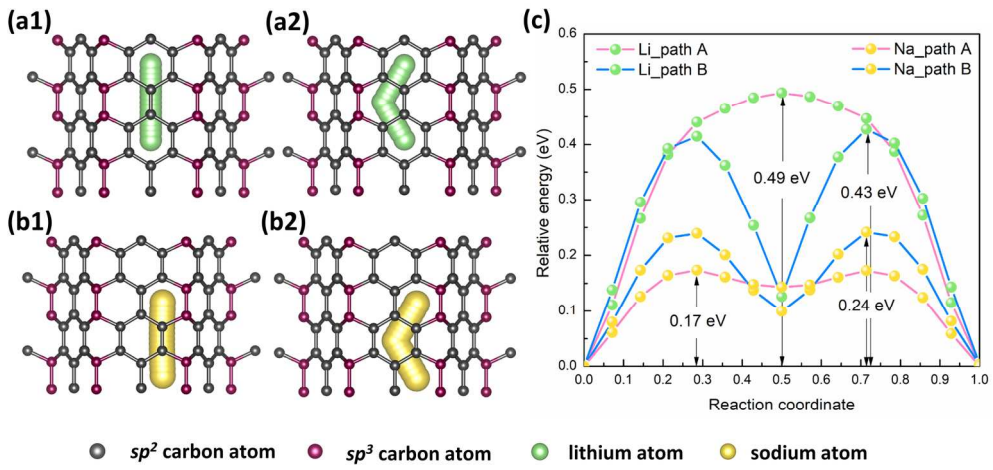

. Lithium migration along C-honeycomb channels following (a1) path A and (a2) path B; sodium migration along C-honeycomb following (b1) path A and (b2) path B; (c) The migration energy barriers for lithium/sodium in C-honeycomb

89x45mm (600 x 600 DPI)